First Order Structure Function Analysis of Statistical Scale Invariance in the AIRS Observed Water Vapor Field

Kyle G. Pressel * and William D. Collins

The University of California, Berkeley, California, USA

Lawrence Berkeley National Laboratory, 1 Cyclotron Road, Berkeley, CA, USA 94720

* *Corresponding author address:* Kyle Pressel, The Department of Earth and Planetary Sciences, Berkeley, CA 94720

E-mail: pressel@berkeley.edu

ABSTRACT

The power law scale dependence, or scaling, of first order structure functions of the tropospheric water vapor field between 58°S and 58°N is investigated using observations from the Atmospheric Infrared Sounder (AIRS). Power law scale dependence of the first order structure function would indicate that the water vapor field exhibits statistical scale invariance. Directional and directionally-independent first order structure functions are computed to assess the directional dependence of derived first order structure function scaling exponents (H) for a range of scales from 50 km to 500 km. In comparison to other methods of assessing statistical scale invariance, the methodology used here requires minimal assumptions regarding the homogeneity of the spatial distribution of data within regions of analysis. Additionally, the methodology facilitates the evaluation of anisotropy and quantifies the extent to which the structure functions exhibit scale invariance.

The spatial and seasonal dependence of the computed scaling exponents is explored. Minimum scaling exponents at all levels are shown to occur proximate to the equator, while the global maximum is shown to occur in the middle troposphere near the tropical-subtropical margin of the winter hemisphere.

From a detailed analysis of AIRS maritime scaling exponents, it is concluded that the AIRS observations suggest the existence of two scaling regimes in the extratropics. One of these regimes characterizes the statistical scale invariance the free troposphere with H approximately 0.55 and a second that characterizes the statistical scale invariance of the boundary layer with H approximately 1/3.

1. Introduction

Generally speaking, a function $f(r)$ exhibits scaling if it has power law dependence on r such that

$$f(r) \propto r^{\alpha} \tag{1}$$

where α is called the scaling exponent. If the function $f(r)$ is a scale dependent statistic of a spatially or temporally distributed field, then scaling is an indicator of the statistical scale invariance of the field. Hereafter, statistical scale invariance will be referred to as scale invariance as is commonly done in the atmospheric science literature. The scaling of atmospheric energy and temperature spectra across a wide range of scales has been well established in the literature (Nastrom and Gage 1985). In particular, Nastrom and Gage (1985) show that observed upper tropospheric wavenumber spectra of wind and temperature have a nearly universal form characterized by two scaling regimes. The first regime occurs within the mesoscale at length scales less than 400 km with a power law scaling exponent of -5/3, while the second regime occurs at scales greater than 400 km with a power law scaling exponent of -3.

Several studies have investigated the scale dependence of water vapor variability and have shown the presence of scaling behavior in water vapor spectra. Nastrom et al. (1986) find that observed water vapor wavenumber power spectra measured by commercial aircraft in the upper troposphere and lower stratosphere follow an approximately -5/3 scaling for scales less than 500 km to 800 km, and that the spectra suggest the existence of a scale break to a steeper scaling at scales greater than 800 km. Tjemkes and Visser (1994) find that water vapor power spectra spectra computed from High-Resolution Infrared Sounder

(HIRS) measurements in the southern hemisphere storm track exhibit an approximately -5/3 wavenumber scaling in both the free troposphere and near surface across a wide range of scales. The scaling of trace gases as observed during the Pacific Exploratory Mission (PEM) has been characterized by Cho et al. (1999). They find that the wavenumber spectra of specific humidity have scaling exponents near -5/3 throughout the depth of the troposphere over scales ranging from 6 km to 60 km. Wood and Taylor (2001) show that water vapor power spectra from aircraft observations made below marine stratocumulus cloud layers exhibit scaling consistent with -5/3 at scales up to 80 km.

There is a growing body of literature that suggests the presence of significant deviations from the -5/3 power spectra scaling suggested by the aforementioned results. Kahn and Teixeira (2009), hereafter KT09, use physical retrievals of water vapor profiles from the Atmospheric Infrared Sounder (AIRS) to compute a global climatology of variance spectra scaling exponents. In particular, they find that maximum values of the spectral scaling exponents occur in the tropical mid-troposphere, and that scaling exponents show significant deviations from $-5/3$ behavior at scales ranging from roughly 100 km to 400 km. Additionally, KT09 find evidence of a very weak scale break that occurs at scales larger that 400 km in water vapor variance spectra, in contrast to the strong scale break they observe in coincident temperature variance spectra. Significant departures from -5/3 scaling behavior are shown by Lovejoy et al. (2010), who find aircraft observations of tropospheric humidity to be consistent with -2 wavenumber scaling from 4 km to 1000 km. Kahn et al. (2011) show that variance spectra for length scales between 10 km and 100 km computed from aircraft transects from the American Monsoon Systems Ocean-Cloud-Atmosphere-Land Study Regional Experiment (VOCALS-REx) exhibit vertical variability, with scaling exponents most

consistent with -5/3 scaling in the near surface and becoming steeper with height.

If water vapor behaves as a passive scalar, and depending on the nature of atmospheric turbulence and the sources and sinks of water vapor, there are two theoretical spectra that may explain the observed spectra. The Obukhov-Corrsin spectrum predicts that passive scalars in locally isotropic turbulent flow will exhibit power spectra scaling with a -5/3 scaling exponent (Corrsin 1951). However, if water vapor acts as a passive scalar forced at large scales, dissipated at small scales, and transported by a two-dimensional velocity field, then in steady state the Batchelor spectrum predicts that wavenumber spectra of such a scalar field should follow a -1 scaling between the forced and dissipative scales (Batchelor 1959; Pierrehumbert 1994). Based on the discussion of prior results, it seems that several of the studies suggest Obukhov-Corrsin type behavior, however, there are several reasons to question such an inference. First, the differences in horizontal and vertical tropospheric length scales suggest that the atmospheric flow field is not isotropic. Second, in several cases (Nastrom et al. 1986; Tjemkes and Visser 1994; Cho et al. 1999) the consistency with -5/3 scaling is confirmed based on comparison to reference spectra rather than explicitly computed scaling exponents, which limits the power of such conclusions. Finally, water vapor is a non-passive scalar interacting with atmospheric motions in a multiplicity of ways, including its role in large scale latent heat transport, its radiative effects as a greenhouse gas, and its enhancement of vertical motions through latent heat release in moist convection (Sherwood et al. 2010).

It is the non-passive nature of water vapor which makes the scaling of water vapor spectra relevant to the subgrid scale representation of moist processes in GCMs and drives the need to further characterize the scale-dependent statistics of the water vapor field. Indeed, the

nonlinear coupling between water in its various phases and the atmospheric flow occurs at all scales of atmospheric motion. The problem of GCM parameterization is one of scale dependence, in that it seeks to couple the simulated climate system to processes operating at scales that cannot be directly resolved by the GCM dynamical core (e.g. Williams (2005)). The scaling of water vapor spectra offers a direct means of connecting small scale variability to large scale variability. Scaling has been proposed as a way of estimating the subgrid scale water vapor variability in GCMs as a basis for statistical cloud parameterization (e.g. KT09, Cusack et al. (1999)) and as a means of comparing GCM representation of the spatial variability water vapor to observed variability (Kahn et al. 2011). Despite the potential utility of observations of scale invariance in climate model development and verification, few studies have characterized the climatology of the scale invariance of the water vapor field.

Scaling of atmospheric spectra have been used to assess climate simulations. Kahn et al. (2011) use variance spectra computed from AIRS physical retrievals and aircraft observations from VOCALS-REx to investigate the consistency between water vapor variance spectra obtained from observations, free-running climate GCMs, and meteorological reanalyses. Their investigations suggest that reanalysis spectra provide better agreement with AIRS observed spectra than GCM spectra. However, in each case the spectral scaling exponents of modeled variance spectra are appreciably larger than observed exponents.

In this paper we compute first order structure function scaling exponents for physical retrievals of water vapor mixing ratio obtained from AIRS. The goals of this paper are to develop a methodology for estimating and interpreting the scaling exponents of water vapor structure functions that also considers the validity of underlying assumptions and the quality of the empirically derived scaling and to apply this methodology to investigate seasonal vari-

ations in the retrieved water vapor field from AIRS. Compared to existing approaches, this methodology introduces greater confidence in the computed exponents and places inferences of universality drawn from these results on a stronger empirical foundation. This paper will proceed by discussing the definition of the structure function in the second section, the AIRS data set in the third section, the computation of directionally-independent and directional structure function scaling exponents in the fourth section, and the climatology of scaling exponents in the fifth section. In the sixth section the results are discussed in the context of the qualitative features of the water vapor field, and a summary and final remarks are given in the seventh section.

2. Structure Functions and Scaling

Most often the scale invariance of observed atmospheric data sets is determined through linear fits to log-log power spectra (log spectra versus log wavenumber) (Nastrom and Gage 1985; Nastrom et al. 1986; Tjemkes and Visser 1994; Cho et al. 1999) or through linear fits to log-log structure functions (log structure function versus log scale)(Pierrehumbert 1996; Marshak et al. 1997; Stolle et al. 2009). In this paper we employ a structure function methodology. The q-th order generalized structure function of a one-dimensional spatially varying field $\phi(x)$ is given by

$$S_q(r) = \langle |\phi(x_i + r) - \phi(x_i)|^q \rangle \tag{2}$$

where $\langle\rangle$ indicates an ensemble mean taken over all pairs of points $(x_i, x_i + r)$ separated by a distance r. The difference inside of the absolute value is typically referred to as an

increment of the field ϕ and is denoted as $\Delta\phi$. The q-th order structure function therefore describes the scale dependence of the expected values of the q-th moment of increments of the field ϕ. In practice, because of the finite size of observational data sets, the ensemble mean in Equation 2 is approximated by the arithmetic mean over a finite the set of observed increments $\Delta\phi$. The Weiner-Khinchin theorem permits the second order structure function scaling exponent to be related to the Fourier power spectra exponent through the relation

$$\beta = -\left(\alpha_2 + 1\right) \tag{3}$$

where β and α_2 are the exponents of the Fourier power spectra and second order structure function, respectively.

In this paper, we compute only the first order structure function scaling exponent, which we refer to as α. The primary reason for analyzing the first order structure function, rather than the second order, is that higher order structure functions are more susceptible to the effects of finite empirical data sets when approximating the ensemble mean in Equation 2 by an arithmetic mean. For some fields whose structure functions of various orders exhibit power law scaling, the scaling exponents of various orders of structure function can be related by the expression

$$\alpha_q = q\alpha \tag{4}$$

where α_q is the q-th order structure function scaling exponent and q is the order of the structure function. In this case, the field is monofractal, and a single scaling exponent is sufficient to completely characterize the scaling of all orders of its structure functions. Fields that exhibit structure function scaling but do not have this property are called multifractal or, synonymously, are said to exhibit anomalous scaling. Many atmospheric fields are known

to exhibit a more complex relationship among the scaling exponents than that given by Equation 4 (e.g. Pierrehumbert (1996); Marshak et al. (1997); Stolle et al. (2009); Cho et al. (2000)). Cho et al. (2000) considered the mesoscale scaling of water vapor structure functions of order 0.5 through 10 as observed by a relatively small number of aircraft flights in the boundary layer and free troposphere. Their findings suggest that, despite clear evidence of anomalous scaling, the approximation described in Equation 2 will provide only a small overestimate (< 0.1) of β. This suggests that $\alpha_2 \approx 2\,\alpha$. Therefore, β can be related to α through Equation 3 by

$$\beta \approx -(2\alpha + 1) \tag{5}$$

as in KT09. To afford comparison to the rather limited prior results, conversion will be made between β and α using Equation 2 when necessary. Independent of the approximation made in Equation 2, α provides considerable descriptive information about spatial correlations in the field ϕ.

The first order structure function scaling exponent (α) provides an efficient means of characterizing the spatial correlative structure of the observed field as an empirical approximation to the Hurst exponent (H), which is widely used to characterize stochastic processes (Hurst 1956). Stochastic processes with $H > 1/2$ exhibit long range correlations and thus the increments of the processes exhibit persistence, in the sense that positive (negative) increments are expected to be followed by further positive (negative) increments. Random processes with $H < 1/2$ do not exhibit long range correlation and the increments of the process are antipersistent in the sense that a positive (negative) increment is expected to be followed by a negative (positive) increment. The Hurst exponent (and, therefore, the

first order structure function exponent) of a one-dimensional random process is related to the fractal dimension D by $D = 2 - H$. Therefore, H characterizes the degree to which the random process fills space. Qualitatively, processes that are more space filling, as indicated by a larger fractal dimension D but smaller Hurst exponent H, are characterized by having a generally rougher appearance (Feder 1988). In the discussion that is to follow we will assume that $H = \alpha$. In order to emphasize their equivalence, throughout the remainder of this paper we will denote first order structure function scaling exponents by H.

For illustrative purposes, examples of two synthetic Gaussian random processes having Hurst exponents of 0.3 and 0.7 are shown in Figure 1, and computed structure functions and fitted power laws for each random process are shown in the inset plots. The random processes were generated using the circulent matrix method described by Wood and Chan (1994). It is clear from the inset structure function plots that both process are characterized by structure functions with power-law behavior and that the process with $H = 0.3$ has a rougher, more space filling appearance, which is characteristic of processes with antipersistent increments, while the process with $H = 0.7$ has a distinctly less space filling and smoother appearance that is characteristic of processes with persistent increments and long range correlations.

In this paper, structure function scaling exponents H are computed from water vapor retrievals from AIRS. Computation and subsequent interpretation of first order structure function exponents estimated from two-dimensional data require the directional dependence of the structure function exponents to be addressed. Unlike time series, which vary only in the temporal dimension, two-dimensional spatially distributed fields may exhibit directional anisotropy resulting in directionally dependent structure functions and scaling exponents. The methodology described herein seeks to investigate the climatology of directionally inde-

pendent and directionally dependent structure function scaling exponents.

3. The AIRS/AMSU Dataset

The AIRS/AMSU instrument suite combines AIRS, a high spectral resolution infrared spectrometer, with the Advanced Microwave Sounding Unit (AMSU) to retrieve the vertical profiles of tropospheric water vapor and temperature. The AIRS/AMSU instrument suite is onboard NASA's sun-synchronous Earth Observing Satellite Aqua (0130 and 1330 local equator crossing times) and collects twice daily observations over most of the planet. AIRS provides physical retrievals of vertical profiles of water vapor mass mixing ratio (q_v) in scenes with up to 70% fractional cloudiness (Aumann et al. 2003). The vertical resolution of AIRS water vapor profiles are dependent on the local meteorological conditions. Maddy and Barnet (2008) estimate that the average vertical resolution is less than or equal to 3 km for all levels below 300 hPa based on analysis of AIRS empirical averaging kernels. Retrievals in partially cloudy scenes are achieved through a cloud clearing methodology as described by Susskind et al. (2003). This methodology combines single AMSU fields of view (FOV) with 3×3 grids of spatially coincident AIRS FOVs to produce cloud cleared radiances used for the subsequent retrieval process.

The spatial resolution of the AIRS data determines the smallest separation r for which we can compute structure functions, and hence it also sets the lower bound on the range of length scales for studies of scaling using these observations. The actual spatial resolution of AIRS observations depends upon the scan geometry and upon atmospheric conditions. Both AIRS and AMSU are cross-track scanning instruments, and therefore the horizontal

spatial resolution degrades from a nominal 45 km-wide footprint (the areal projection of the instrument aperture on the Earth's surface) at nadir to a 150 km-wide footprint at the extremes of the scan lines (Aumann et al. 2003). Furthermore, the cloud clearing methodology eliminates some fraction of the 9 AIRS coincident FOVs per AMSU FOVs that are impacted by cloudiness, thereby making the effective resolution for each retrieval dependent on cloud fraction (Susskind et al. 2003).

AIRS physical retrievals have been the subject of several validation studies, including comparisons against Atmospheric Radiation Measurement (ARM) site observations (Tobin et al. 2006), dropsondes (Pu and Zhang 2010), radiosondes (Hagan et al. 2004; Divakarla et al. 2006), and aircraft measurements (Hagan et al. 2004; Gettelman et al. 2004). Validation studies have shown that AIRS performs to within the design error tolerance of less than 20% RMS error for water vapor mass mixing ratio observations. See KT09 for a more detailed discussion of AIRS validation.

For this study we use physical retrievals of water vapor mass mixing ratio from the AIRS Version 5 Level 2 Standard Product for December, January and February (DJF) in 2007 and 2008 and June, July and August (JJA) in 2008. Structure functions for ascending (daytime) and descending (nighttime) overpasses are computed separately in order to quantify the sensitivity of scaling to diurnal variations. Gettelman et al. (2004) have shown that AIRS loses sensitivity above 200 hPa where water vapor concentrations fall to less than 10 ppmv. Therefore, we limit the range of this study to pressure levels between 1000 hPa and 300 hPa to ensure the accuracy of the results. The AIRS data are quality controlled using the *PGood* quality indicator, which identifies retrievals that are of sufficient quality for statistical climate studies but may not be suitable for assimilation (Olsen et al. 2007). Negative water vapor

mixing ratio retrievals are excluded from the analysis. Additionally, as suggested by Olsen et al. (2007), we require that the estimated standard error of the retrieval be less than 50% of the retrieved value. In order to minimize any bias towards dry conditions in the data set, no additional cloud masking is used in this study beyond the cloud screening already employed in the AIRS retrieval process.

Figures 2 and 3 show the AIRS three month mean water vapor retrievals for ascending (daytime) and descending (nighttime) overpasses at 925 hPa and 500 hPa, respectively. In order to conform with the AIRS pressure level convention, quantities reported on pressure levels in this paper represent the mean values of those quantities between the stated level and the adjacent level above (in physical space). For example, water vapor retrievals reported at 925 hPa represent the mean water vapor mixing ratio between 925 hPa and 850 hPa. At both pressure levels the maximum values of water vapor mixing ratio occur in the ascending branch of the tropical circulation. At 500 hPa there is evidence of a subtropical minimum of water vapor mass mixing ratio associated with the subsidence branch of the mean Hadley circulation. There is a decrease in water vapor mixing ratio away from the tropics, which can be directly associated with the dependence of saturation mixing ratio on temperature as predicted by the Clausius-Clapeyron equation.

4. Computation of Structure Functions and Scaling Exponents from AIRS Data

For an arbitrary scalar field $\phi(\mathbf{x})$ of a two-dimensional argument $\mathbf{x} \in \mathbb{R}^2$ the first order generalized structure function is given by

$$S_1(\mathbf{x}, \mathbf{r}; \phi) = \langle |\phi(\mathbf{x} + \mathbf{r}) - \phi(\mathbf{x})| \rangle \tag{6}$$

where $\langle\rangle$ indicates an ensemble mean taken across all pairs of points $(\mathbf{x} + \mathbf{r}, \mathbf{x})$ for a large number of realizations of the field $\phi(\mathbf{x})$. The structure function exhibits scaling in a direction $\theta = \arccos \frac{(\mathbf{r} \cdot \mathbf{x})}{||r|| ||x||}$ if

$$S_1(\mathbf{x}, \mathbf{r}; \phi) \propto ||r||^{\alpha(\mathbf{x}, \theta)} \tag{7}$$

where $\alpha(\mathbf{x}, \theta)$ is the power law scaling exponent at $\mathbf{x}$ in the direction θ.

If the field exhibits statistical spatial homogeneity and isotropy, then Equation 6 loses dependence on the orientation of position $\mathbf{x}$ and separation $\mathbf{r}$ and can be simplified to

$$S_1(r; \phi) = \langle |\phi(\mathbf{x} + \mathbf{r}) - \phi(\mathbf{x})| \rangle \tag{8}$$

where the ensemble mean $\langle\rangle$ is now taken over all points separated by a lag distance $r = ||\mathbf{r}||$. In this case, the field exhibits scaling of the first order structure function if

$$S_1(r; \phi) \propto r^{\alpha}. \tag{9}$$

Recall that α (whether directionally dependent or independent) is considered to be equivalent to the Hurst exponent H in our analysis.

Previous analysis of variance scaling of the AIRS observed water vapor fields has implicitly assumed that the variance field is homogeneous and isotropic at scales of up to $12^\circ \times 12^\circ$

in latitude and longitude (KT09). In order to quantify the anisotropy of structure function scaling we compute three separate structure functions. One structure function is computed from increments regardless of direction (directionally independent), a second from increments that are oriented in the direction of the satellite track (along-track), and a third for increments that are oriented normal to the satellite track (across-track). The along-track direction is oriented in a North-South direction as the ascending (descending) equator crossing occurs with an angle of 8° west of North (8° east of South).

Structure functions and scaling exponents are computed for overlapping domains centered every two degrees globally from 58°S to 58°N. The domains extend $12° \times 12°$ in latitude and longitude at the equator and increase in longitudinal width away from the equator in order to keep the area of the domain approximately constant. The choice of domain size ensures that there are a sufficient number of increments of each lag distance to provide an approximation of the ensemble mean. Structure functions are computed by binning water vapor increments by lag distance r, where the lag distance for an increment is defined as the great circle distance between the locations of the retrievals composing the increment. Increments are accumulated for the entire period of analysis and are used to compute a single structure function for each domain. Structure functions are computed over a range of lag-distance bins that are non-overlapping and centered every 50 km between 50 km and 500 km inclusive. Figure 4 shows example along-track, across-track, and directionally independent structure functions. For the directionally-independent structure functions all increments, independent of direction, are binned by lag-distance, while in the case of cross-track (along-track) structure functions only increments which are normal (parallel) to the satellite ground track are binned. Finally, the arithmetic mean is computed for each bin

in order to approximate the structure function. Structure function scaling exponents are determined by least squares fit to the log-log structure function between 50 km and 500 km. The range of scales has been selected to avoid relatively weak scale-breaks which had been observed in previous studies (KT09).

The exponent for each domain is then gridded according to the latitude and longitude of the domain center and plotted as a map. It is important to note that the exponents computed for each domain are estimated using data which are also used to compute scaling exponents for adjacent partially overlapping domains, and hence the exponents plotted on each map are not truly independent for separations smaller than half of the domain size.

In order to analyze the climatology of structure function scaling exponents it is necessary to identify structure functions exhibiting power law scale dependence. Two methods for identifying structure functions with power law scaling have been tested. The first method identifies structure functions as scaling when the ratio of the width of the linear regression slope parameter confidence interval to the regression slope itself is within an empirically-determined percentage threshold (Tuck 2010). Due to the small number of degrees of freedom in the regression (the number N of lag distances $-$ 2), and since the width of the confidence interval is proportional to $1/\sqrt{N-2}$, this test tends to reject a large number of log-log structure functions for reasonable choices of the confidence interval width despite satisfactory linearity over the scaling range. We have considered an alternate method based upon setting an ad hoc lower bound on the coefficient of determination (R^2). This is mathematically equivalent to setting a minimum amount of the variance of the log-log structure function that is required to be explained by the linear regression in order for the structure function to be deemed as scaling. Tests have shown that the second method is successful in identifying

scaling structure functions, and we adopt this alternate method with a lower bound on R^2 of 0.95 for the remainder of our analysis.

As previously mentioned, this study involves two periods of analysis, the first in boreal winter during December, January, and February of 2007 and 2008 and the second in boreal summer during June, July, and August of 2008. Over each period, increments are computed from each day's data. Then, the increments obtained on each day are combined to compute a single structure function for the entire three month period for each $12^\circ \times 12^\circ$ domain. Combining increments over the entire period to compute a single structure function and scaling exponent requires the assumption that the increments are being sampled from a temporally statistically stationary field. It was found that a three month analysis period provided sufficient sampling to allow robust estimation of the ensemble means required by the structure functions.

5. Results

a. Maps of Scaling Exponents

Maps of structure function scaling exponents (H) over scales ranging from 50 km to 500 km computed from AIRS water vapor mass mixing ratio retrievals for the 500 hPa and 925 hPa levels for DJF 2007/2008 and JJA 2008 are shown in Figures 5 and 6, respectively. The scaling exponents for each $12^\circ \times 12^\circ$ domain have been plotted regardless of the $R^2 > 0.95$ quality of fit criterion. However, regions for which the $R^2 > 0.95$ quality of fit criterion is not met are indicated with black hatching. The near absence of hatching in the directionally-

independent and across-track maps (the left two columns of Figures 5 and 6) suggests the presences of nearly ubiquitous structure function scaling. The exceptions to the nearly ubiquitous scaling of directionally-independent and across-track structure functions occur primarily in a few regions of the deep tropics for both 500 hPa and 925 hPa and at the northern and southern extremes of the domain of analysis for the 925 hPa level. The along-track scaling exponent maps indicate similar behavior for the along-track structure function in the subtropics and midlatitudes with nearly ubiquitous scaling behavior, but suggest the occurrence of widespread departures from structure function scaling in the tropics where the $R^2 > 0.95$ criterion is not met. The maps also suggest that there is a slight diurnal variation in the aerial coverage of the hatched regions, with the largest areal coverage occurring for the ascending (daytime) overpasses.

The coloration of the maps shown in Figures 5 and 6 has been intentionally selected to draw clear distinction between $H < 0.5$ and $H > 0.5$ scaling behavior. Cool colors are used to indicate $H < 0.5$ behavior and warm colors are used to indicate $H > 0.5$ behavior. It is then apparent that the most dominant feature of the maps is the distinction that can be made between the $H > 0.5$ behavior at 500 hPa and the $H < 0.5$ behavior at 925 hPa that is clearly apparent in the subtropics and midlatitudes. Additionally, in the directionally-independent and across-track cases, it is evident that a second obvious distinction can be made between equatorial scaling exponents with $H > 0.5$, on one hand, for subtropical and midlatitude exponents and $H < 0.5$ for tropical scaling exponents, on the other.

The similarities between directionally-independent, along-track and across-track scaling exponent maps for each case (across each row in Figures 5 and 6) suggest that the scaling is approximately isotropic, particularly outside of the tropics. Comparing the ascending

(daytime) and descending (nightime) maps suggests the presence of some diurnal variation in scaling exponents, with larger diurnal variation of directional scaling exponents than of directionally-independent scaling exponents. Comparing the maps in Figure 5 with those in Figure 6 indicates that there is strikingly little seasonal variability in the scaling exponent maps, with the general qualitative features remaining very similar between DJF and JJA. The most notable and obvious exception to the limited seasonal variation is the region of $H < 0.5$ at 500 hPa that appears in conjunction with the South Asian Monsoon during JJA. Additionally, the maps provide some evidence of a slight shift southward of the tropical $H < 0.5$ region at 500 hPa from DJF to JJA.

Very few studies have considered the spatial variability of scaling exponents. Therefore, there are a limited number of prior analyses to which these results can be compared. KT09 show maps of AIRS variance spectra scaling exponents on the 850 hPa and 300 hPa levels for two seasons, MAM and SON, making direct comparison to these results difficult. Nonetheless, the most obvious distinction between the maps shown here and those in KT09 is the lack of a distinct equatorial minimum in scaling exponents as has been observed here. However, the results do confirm the findings of KT09 and Lovejoy et al. (2010) that there are significant departures from the $H \approx 1/3$ ($\beta = -5/3$) behavior described by Nastrom et al. (1986) and Tjemkes and Visser (1994) across a similar range of scales as those reported here.

b. Zonal Mean Cross Sections

The zonal symmetry evident in the maps of scaling exponents shown in Figures 5 and 6 suggests the appropriateness of computing zonal means. Figure 7 shows zonal mean cross sections of maritime directionally-independent (left column), along-track (center column), and across-track (right column) scaling exponents computed for all AIRS layers between 1000 hPa and 300 hPa. The computation of zonal means has been limited to include only those exponents from maritime structure function domains (those having a land fraction less than 0.1) in order to avoid the effects of varying surface topography on the lower tropospheric zonal means, and hence are referred to as maritime zonal means. Additionally, in order to only include domains for which there is evidence of structure function scaling, only domains for which the $R^2 > 0.95$ quality of fit criterion is met are included in the computation of the zonal mean. Therefore, latitudes for which the $R^2 > 0.95$ criterion is not frequently met should be interpreted with substantial caution. We note that that the systematic breakdown of scaling of the along-track structure function in proximity to the equator is a robust feature at all pressure levels, and thus caution against attempts at interpretation of zonal means of along-track structure function scaling exponents within 15° of the equator at all pressure levels.

As with the maps shown previously, the coloration of the zonal mean cross sections shown in Figure 7 has been selected in order to draw a clear distinction between $H < 0.5$ and $H > 0.5$ scaling behavior. It is apparent from the plots that $H > 0.5$ characterizes the water vapor field in the midlatitude, subtropical, and non-equatorial tropical free troposphere at levels above 850-700 hPa and that $H < 0.5$ characterizes the water vapor field in the near surface

and in the equatorial tropics at all levels. The location of the maximum zonal mean scaling exponent for each case is indicated with a black cross in Figure 7, and typically occurs in the winter hemisphere near the margin between the tropics and subtropics at the 400 hPa or 500 hPa level. Poleward of 20° in each hemisphere the zonal mean directionally-independent and directional scaling exponents are similar, but the directional structure functions tend to be slightly larger than their directionally-independent counterparts.

There is clear evidence of diurnal variation in the near surface, which is apparent in Figure 7 as a downward migration of the 0.4 contour line between the ascending (daytime) and descending (nighttime) cases. The diurnal variation is approximately hemispherically symmetric for DJF, but during JJA the diurnal variation appears stronger in the northern hemisphere. We also note that the zonal mean directional structure functions exponents have a larger diurnal variation in the free troposphere than the directionally-independent structure function exponents. The causes of this difference are unknown. The amplified diurnal variation of directional scaling exponents is largest in the across-track direction, and appears to mostly be related to increases in ascending pass (daytime) exponents leading to a larger apparent anisotropy for ascending pass exponents. Whatever the cause of the daytime anisotropy, by comparison the descending pass zonal means are indicative of considerably more isotropic conditions. Inspection of the 0.5 contour lines in Figure 7 shows that they do not undergo the same downward shift observed for the 0.4 contour lines. This suggests that, despite the observed diurnal variations in exponents, the relative apportionment of $H < 0.5$ and $H > 0.5$ fractional area coverage does not undergo a significant variation.

The diurnal cycle evident in the maritime zonal mean scaling exponents on the 1000 hPa and 925 hPa levels appears as a shift from values near 1/3 during the daytime to values

closer to 0.4 at night (this is particularly evident in the probability density estimates shown in Figure 9, which will be discussed in more detail later), which is similar to the variation of scaling exponents across the top of the planetary boundary layer. Pressel et al. (2010) show that water vapor variance spectra observed at the 396 m level of a tall tower display a nocturnal increase in scaling exponents reminiscent of that evident in the AIRS zonal means. Similarly, Kahn et al. (2011) show water vapor variance spectra scaling exponents of 0.32 for VOCALs-REx flight segments below 700 m, with exponents increasing to 0.45 above 3000 m at scales ranging from 10 km to 100 km. Additionally, Cho et al. (2000) found a similar vertical variability at scales up to 100 km with scaling exponents varying from values near 0.25 in the boundary layer to higher free tropospheric values of 0.37 and 0.44 in the tropics and extratropics, respectively. Given these corroborating results, it is tempting to explain the AIRS observed diurnal variations as the results of diurnal variations in the planetary boundary layer. However, the vertical resolution of AIRS retrievals is dependent on the atmospheric vertical temperature gradient, which within the boundary layer undergoes significant diurnal variation and precludes a simple interpretation of the diurnal variation of boundary layer scaling exponents in terms of variations in boundary layer structure.

AIRS effective averaging kernels are a means of quantifying the retrieval vertical resolution (Maddy and Barnet 2008). Effective averaging kernels are included in the AIRS Level 2 support product. The effective averaging kernels provide a measure of the vertical correlation in retrieved properties and hence provide a means of estimating the vertical extent over which a retrieval at a particular level exhibits sensitivity (Maddy and Barnet 2008). The empirical averaging kernels do not necessarily sum to unity and significant departures from unity indicate dependence on the first guess used in the AIRS retrieval and loss of instrument

sensitivity. Figure 8 shows mean averaging kernels for 2° latitude longitude boxes centered at (31°N, 90°W), (0°N, 0°W), and (30°N, 50°W), which we use to represent the qualitative characteristics of subtropical land, tropical ocean, and subtropical ocean averaging kernels respectively. The mean averaging kernels represent the arithmetic mean of averaging kernels for the 925 hPa, 700 hPa, and 500 hPa AIRS layers for all water vapor retrievals within the 2° latitude-longitude box during the DJF and JJA periods. In order to characterize the diurnal variation of AIRS vertical resolution and sensitivity, separate mean averaging kernels are reported for ascending and descending passes.

The mean averaging kernels in Figure 8 are intended to provide qualitative insight into the vertical resolution of the AIRS retrievals; more quantitative analysis would be useful but is not required to support the primary effects summarized here. There are two primary features to note in Figure 8. First, there is a greater difference between ascending and descending pass mean averaging kernels at 925 hPa than at the other two levels. The shift to smaller values of the averaging kernel at night indicates a decrease in AIRS sensitivity from day to night. The change in sensitivity is likely related to diurnal variations in the lower tropospheric temperature profile. The nocturnal decrease in sensitivity appears to be more significant over land than over sea. Given that diurnal variations in the depth of the maritime boundary layer are typically rather small, we speculate that the observed diurnal variation in scaling exponents is a result of changes in the sensitivity of AIRS to variations in the near surface water vapor field. Second, it is apparent that the mean averaging kernels for the 700 hPa layer, which remain greater than zero below 925 hPa, suggest that for all cases water vapor retrievals are sensitive to water vapor fluctuations in the near surface. This suggests that the slow increase in mean scaling exponents from the near surface to the

free troposphere that is evident in Figure 8 is likely related to the finite vertical resolution of AIRS and that AIRS profiles lack the vertical resolution necessary to resolve any abrupt transition that may occur at the top of the boundary layer. The 500 hPa averaging kernels appear to be predominantly independent of water vapor variations below 850 hPa, suggesting that 500 hPa retrievals are representative of the free troposphere.

c. Probability Density Estimates and Universality

The averaging kernels shown in Figure 8 suggest that the relatively smooth vertical variation in scaling exponents evident in the zonal mean cross-sections between the near surface (1000 hPa and 925 hPa) and the free troposphere (500 hPa, 400 hPa, and 300 hPa) may be the result of an inability of the AIRS retrievals to resolve abrupt transitions at the top of boundary layer. We therefore separate the remainder of the analysis into two distinct scaling regimes that the averaging kernels suggest are largely independent and are representative of the free troposphere and near surface. We take exponents computed on the 500 hPa and 925 hPa levels to be representative of the free troposphere and near surface, respectively. Given that the averaging kernels shown in Figure 8 suggest that the 925 hPa level exhibits mean diurnal thermodynamic variability, which is likely the source of changes in the instrument sensitivity, we will henceforth refer to the 925 hPa level as being representative of the boundary layer regime.

Probability density estimates of directionally independent maritime extratropical (poleward of 20°N and 20°S) scaling exponents from domains with nearly isotropic scaling and satisfying the $R^2 > 0.95$ quality of fit criterion are shown in Figure 9 for the 925 hPa and

500 hPa levels. Similar to the zonal means shown previously, the PDFs are computed from only maritime exponents. In order to limit the analysis to domains with nearly isotropic scaling, we require that the difference between along- and across-track scaling exponents be no more than 10% of the directionally-independent scaling exponent. Sensitivity tests suggest that both the distribution shape and statistics are relatively insensitive to the value of the anisotropy threshold over a range from 5% to 50%. Constraining the current analysis to nearly isotropic maritime extratropical scaling exponents serves two purposes: first, to remove the effects of topographic heterogeneities from the analysis and, second, to limit the effects of anisotropic scaling on the interpretation of directionally-independent exponents. Table 1 summarizes statistics of the exponent distributions shown in Figure 9 and also gives the percentage of maritime extratropical structure function exponents exhibiting nearly isotropic scaling. The table indicates that, with the exception of the DJF 925 hPa ascending case, the majority of extratropical structure function domains exhibit directionally-independent structure function scaling exponents. Therefore, density estimates shown in Figure 9 summarize the frequency distribution of structure function exponents for which there is strong evidence of scaling behavior (based on the R^2 criterion) and strong evidence of directionally-independent scaling exponents (based on the anisotropy threshold), conditions which characterize a large portion of the atmosphere.

The density estimates for the 925 hPa level, which are representative of the boundary layer regime, are shown in the left panel of Figure 9. The displacements between solid and dashed lines of the same color are indicative of the diurnal variation in scaling exponents. Results of the averaging kernels analysis suggest that AIRS is most sensitive to boundary layer water vapor during ascending passes, and hence we will limit our discussion of the boundary

layer scaling exponent frequency distributions to ascending (daytime) passes. The density estimates of daytime boundary layer regime estimates are unimodal with a peak occurring very near 1/3 ($\beta = -5/3$) for both DJF and JJA. The 95% bootstrapped confidence interval reported in Table 1 for DJF and JJA mean scaling exponents ($\bar{H}$) are $0.333 \leq \bar{H} \leq 0.337$ and $0.332 \leq \bar{H} \leq 0.336$ respectively. The bootstrapped confidence intervals are perhaps optimistically small as the scaling exponents are computed for structure function domains that are partially overlapping and hence not entirely independent. Nevertheless, we argue that given the independence of the DJF and JJA results, there is high confidence that $\bar{H}$ is near 1/3 over a range of scales from 50 km to 500 km.

There are relatively few studies that investigate scaling of water vapor over the range of scales from 50 km to 500 km to which the $\bar{H} \approx 1/3$ result can be compared. Perhaps the best comparison is to the results of KT09, who show near surface variance spectra scaling exponents to be roughly consistent with the $\bar{H} \approx 1/3$ behavior shown here and are similarly found to be consistent with the findings of Tjemkes and Visser (1994). Other studies have shown similar statistical scaling behavior, albeit over length scales typically shorter than 100 km (e.g. Cho et al. (2000); Wood and Taylor (2001); Comstock et al. (2005); Kahn et al. (2011)). These earlier results, taken in conjunction with the new results, appear to present building evidence of nearly universal $H = 1/3$ scaling at scales from below 50 km to 500 km in the boundary layer.

Scaling exponent density estimates for the 500 hPa level, which are taken to be representative of the free tropospheric regime, are shown in the right panel of Figure 9. The free tropospheric regime density estimates peak at 0.5. Table 1 shows that based on the bootstrapped 95% confidence interval, $\bar{H}$ likely lies in the range $0.546 \leq \bar{H} \leq 0.562$ for all cases,

including both ascending and descending overpasses in DJF and JJA. Like the boundary layer regime, there is remarkably little seasonal variation in the observed exponents, which lends confidence in the precision of the result.

As in the boundary layer regime, there are relatively few results to which the free tropospheric regime results can be compared. These results confirm the general results of KT09, who report variance scaling exponents as large as 0.5-0.6 in some areas of the subtropical free troposphere. Moreover, the results reported here are found to support the results of Lovejoy et al. (2010), who estimated $H = 0.51$ for the free tropospheric humidity field. The free tropospheric regime results are found not to agree with the free tropospheric results of Nastrom et al. (1986) or Tjemkes and Visser (1994), who report scaling exponents that are more consistent with $H \approx 1/3$ behavior.

6. Discussion

As is evident in Figure 1, the behavior of fields characterized by $H > 0.5$ and those characterized by $\mathrm{H} < 0.5$ are tangibly different. Therefore, it is prudent to ask if there are qualitative features for of the observed field that can provide a mechanistic explanation the vertical and horizontal distributions of exponents observed by this study. Structure functions are computed from spatial increments of the instantaneous water vapor field, hence the three month means shown in Figures 2 and 3 are not particularly useful for interpreting structure function behavior. Therefore, in Figure 10 are shown maps of water vapor mixing ratio from a single day's ascending passes for the 500 hPa and 925 hPa levels. These maps are taken to be representative of the instantaneous water vapor field. The quantity plotted in Figure

10 is the logarithm of the normalized water vapor mass mixing ratio, where the mixing ratio has been normalized by its global maximum value for each level. This normalization allows the plots to share a common colorbar and makes extratropical spatial gradients more visible. The two days shown in Figure 10 were not selected for any particular purpose other than to offer an example of the instantaneous water vapor field for both winter and summer seasons.

The left two panels of Figure 10 show the 500 hPa water vapor field. Perhaps the most striking features of the 500 hPa field are the filamentary structures that extend from the deep tropics into the midlatitudes. The filamentary structures are emblematic of large scale two-dimensional chaotic mixing (e.g. Pierrehumbert and Yang (1993); Yang and Pierrehumbert (1994)). Yang and Pierrehumbert (1994) show that chaotic mixing processes in the free troposphere rapidly generate a wide spectrum of moisture filaments, and that within the midlatitudes these filaments lead to a fractal (i.e. H¿0) moisture field. They show that moisture filaments are initially generated by extrusion of moist air from the tropics through a partially permeable tropical mixing barrier. Within the tropics they show that the impediment to rapid exchange of moist tropical air with drier extra tropical air presented by the mixing barrier lead to a more homogeneous tropical water vapor field that does not exhibit fractal behavior (i.e. $H = 0$). Our results are largely consistent with both of these results, as we have shown clear $H > 0$ behavior throughout the extratropics that is clear evidence of fractal behavior. Additionally, we have shown a marked decrease in directionally-independent and across track scaling exponents in the tropics in conjunction with a systematic breakdown of along track structure function scaling.

We propose that the spectrum of filaments generated by chaotic mixing is responsible for the $H > 0.5$ free tropospheric behavior observed in this study. Chaotic mixing has been

identified as important in determining the scaling of stratospheric scalar spectra (e.g. Haynes and Vanneste (2004)). Additionally, filamentary structures similar to those apparent in the water vapor field have been described in stratospheric scalar fields (e.g. Waugh (1996)) and numerous studies have shown these fields exhibit $H \approx 1/2$ scaling behavior at scales from 50 km to 500 km (e.g. Tuck and Hovde (1999),Tuck et al. (1999),Sparling and Bacmeister (2001)). In particular, Tuck and Hovde (1999) estimate H for stratospheric ozone field and found its mean, $\bar{H}$ = 0.56, which is strikingly similar to the values for $\bar{H}$ reported for the water vapor field given in Table 1.

Considering the boundary layer regime, for which relevant instantaneous water vapor fields are shown in the right most panels of Figure 10, it is evident that while the boundary layer water vapor field is not completely devoid of filamentary type structures, they are considerably less distinct. This is likely a result of the fact that the existence of large scale gradients in the boundary layer water vapor field, similar to the gradients observed in the free troposphere, would be indicative of significant disequilibrium between the atmosphere and surface sources of water vapor. Hence, the large horizontal water vapor gradients associated with filamentary type structure are damped by fluxes of water vapor into the atmosphere from the surface. This allows local variations in the boundary layer to play a more dominant role in establishing the spatial variability of water vapor than is done by the large scale flow. While we do not propose a mechanism by which the boundary layer achieves the $\bar{H} \approx 1/3$ scaling of water vapor structure functions, it is apparent that the results of Wood and Field (2011) underscore the complicated interrelationship between boundary layer clouds and the water vapor field.

7. Summary and Final Remarks

In this paper we have described a method for computing first order structure function scaling exponents from physical retrievals of water vapor mass mixing ratio from AIRS. Three separate first order structure functions are computed as part of the analysis, namely the directionally independent, across satellite track, along satellite track structure functions. The three separate structure functions allow investigation of the directional dependence of the observed scaling. A threshold on the coefficient of determination of $R^2 > 0.95$ for the least squares fit to log lag versus distance log structure function is used to identify structure functions that exhibit power law scaling behavior.

The method is used to compute maps of structure function scaling exponents and zonal mean cross sections of maritime structure function scaling exponents for constant pressure surfaces ranging from 1000 hPa to 300 hPa between 58°S and 58°N. It is shown that directionally-independent and across-track structure functions exhibit nearly ubiquitous scaling while along-track structure functions tend not to exhibit scaling in equatorial regions. The maps and zonal means both suggest the presence of an equatorial minimum in scaling exponents at all levels. Outside of equatorial regions, both the maps and zonal means suggest the scaling exponents exhibit significant vertical variability, ranging from 0.3 in the near surface to values greater than 0.5 in the middle troposphere. Investigation of AIRS averaging kernels lead to the identification of two scaling regimes, one which characterizes boundary layer variability and a second which characterizes free tropospheric variability. The peaks in the probability density estimates of daytime boundary layer regime scaling exponents occur near 0.33 and transition to slightly larger values at night. The peaks in the

probability density estimates of free tropospheric scaling exponents occur near 0.55 in both DJF and JJA cases and show significantly less diurnal variation than their boundary layer counterparts.

Therefore the extremely narrow confidence intervals, the agreement between DJF and JJA density estimates, and the agreement with prior results, indicates growing evidence that $\bar{H} \approx 1/3$ provide a relatively universal characterization of boundary layer structure function scaling poleward of 20° in each hemisphere at scales from below 50 km to at least 500 km. This result has several significant implications. First, the scale-invariance implied by the nearly isotropic scaling of structure functions indicates that AIRS observed scale dependent spatial variability may be extrapolated to smaller scales. A similar conclusion has been drawn by KT09. Second, there is strong empirical support for GCM parameterizations that seek to represent sub-grid scale variability based on the downscaling of grid scale variability (e.g. Cusack et al. (1999)), given that the model grid scales provide an accurate estimate of grid scale variability. Third, recent work by Wood and Field (2011), shows that the distribution of cloud horizontal sizes, power law scaling with an approximately -5/3 exponent across scales ranging from 0.1 km to 1500 km. They propose a bounded cascade model that assumes the water vapor field exhibits scale-invariance characterized by $H = 1/3$, and the results reported here offer significant support for this modeling assumption.

Additionally, there is significant confidence that free tropospheric water vapor field exhibits behavior with $H > 0.5$. We argue that this is explained by the generation of filimentary structures in the water vapor field that are the result of chaotic mixing processes as described by Yang and Pierrehumbert (1994)

The structure functions analysis reported herein has been limited to the first order struc-

ture function, but extension to other orders of structure functions may provide a fuller characterization of the scale dependence of water vapor variability. Also, structure functions are estimates of the moments of scale dependent increment probability density functions (PDFs), analysis of the climatology of these PDFs directly may prove fruitful in understanding the underlying stochastic process that generate the observed scale dependence, and provides another means of inter comparing observations and simulation. The success of this methodology suggests that its application to other AIRS retrieved fields may provide further insight into the the scale invariance of atmospheric fields.

Acknowledgments.

This work was supported by the Director, Office of Science, Office of Biological and Environmental Research, Climate Change Research Division, of the U.S. Department of Energy under Contract No. DE-AC02-05CH11231 During the course of this research KGP was supported by The NASA Interdisciplinary Science Program and the DOE BER project on robust regional climate modeling. WDC was supported by Contractor Supporting Research (CSR) funding from Berkeley Lab, provided by the Director, Office of Science, of the U.S. Department of Energy under Contract No. DE-AC02-05CH11231 and the DOE BER project on robust regional climate modeling. The authors would like to thank Brian Kahn and Farid Ait-Chaalal for productive discussions and suggestions and the two reviewers for their comments, criticisms, and suggestions that yielded significant improvements in the manuscript. AIRS data were obtained through the Goddard Earth Sciences Data and Information Services Center (online at http://daac.gsfc.nasa.gov/).

REFERENCES

Aumann, H., et al., 2003: AIRS/AMSU/HSB on the Aqua mission: Design, science objectives, data products, and processing systems. *Geoscience and Remote Sensing, IEEE Transactions on*, **41 (2)**, 253–264.

Batchelor, G. K., 1959: Small-scale variation of convected quantities like temperature in turbulent fluid. Part 1. General discussion and the case of small conductivity. *Journal of Fluid Mechanics*, **5 (01)**, 113–133.

Cho, J., R. Newell, and J. Barrick, 1999: Horizontal wavenumber spectra of winds, temperature, and trace gases during the Pacific Exploratory Missions: 1. Climatology. *J. Geophys. Res*, **104 (D5)**, 5697–5716.

Cho, J., R. Newell, and G. Sachse, 2000: Anomalous scaling of mesoscale tropospheric humidity fluctuations. *Geophys. Res. Lett.*, **27 (3)**, 377–380.

Comstock, K., C. Bretherton, and S. Yuter, 2005: Mesoscale variability and drizzle in southeast Pacific stratocumulus. *J. Atmos. Sci.*, **62 (10)**, 3792–3807.

Corrsin, S., 1951: On the spectrum of isotropic temperature fluctuations in an isotropic turbulence. *Journal of Applied Physics*, **22 (4)**, 469–473.

Cusack, S., J. Edwards, and R. Kershaw, 1999: Estimating the subgrid variance of saturation, and its parametrization for use in a GCM cloud scheme. *Quart. J. Roy. Meteor. Soc.*, **125 (560)**, 3057–3076.

Divakarla, M., C. Barnet, M. Goldberg, L. McMillin, E. Maddy, W. Wolf, L. Zhou, and X. Liu, 2006: Validation of Atmospheric Infrared Sounder temperature and water vapor retrievals with matched radiosonde measurements and forecasts. *J. Geophys. Res.*, **111**, D09S15.

Feder, J., 1988: *Fractals*. Plenum Press, 283 pp.

Gettelman, A., et al., 2004: Validation of Aqua satellite data in the upper troposphere and lower stratosphere with in situ aircraft instruments. *Geophys. Res. Lett.*, **31**, L22 107.

Hagan, D., et al., 2004: Validating AIRS upper atmosphere water vapor retrievals using aircraft and balloon in situ measurements. *Geophys. Res. Lett.*, **31 (21)**, L21 103.

Haynes, P. and J. Vanneste, 2004: Stratospheric tracer spectra. *Journal of the atmospheric sciences*, **61 (2)**, 161–178.

Hurst, H., 1956: Methods of using long-term storage in reservoirs. *ICE Proceedings*, Vol. 5, 519–543.

Kahn, B. and J. Teixeira, 2009: A global climatology of temperature and water vapor variance scaling from the Atmospheric Infrared Sounder. *J. Climate*, **22 (20)**, 5558–5576.

Kahn, B., et al., 2011: Temperature and water vapor variance scaling in global models: Comparisons to satellite and aircraft data. *J. Atmos. Sci.*, **68**, 2156–2168.

Lovejoy, S., A. Tuck, and D. Schertzer, 2010: Horizontal cascade structure of atmospheric fields determined from aircraft data. *J. Geophys. Res*, **115**, D13 105.

Maddy, E. and C. Barnet, 2008: Vertical resolution estimates in version 5 of AIRS operational retrievals. *Geoscience and Remote Sensing, IEEE Transactions on*, **46 (8)**, 2375–2384.

Marshak, A., A. Davis, W. Wiscombe, and R. Cahalan, 1997: Scale invariance in liquid water distributions in marine stratocumulus. Part II: Multifractal properties and intermittency issues. *J. Atmos. Sci.*, **54 (11)**, 1423–1444.

Nastrom, G. and K. Gage, 1985: A climatology of atmospheric wavenumber spectra of wind and temperature observed by commercial aircraft. *J. Atmos. Sci.*, **42**, 950–960.

Nastrom, G., W. Jasperson, and K. Gage, 1986: Horizontal spectra of atmospheric tracers measured during the Global Atmospheric Sampling Program. *J. Geophys. Res*, **91 (D12)**, 13 201–13 213.

Olsen, E., E. Fishbein, T. Hearty, S. Lee, F. Irion, B. Kahn, and E. Manning, 2007: AIRS version 5 release level 2 standard product quickstart. `http://disc.sci.gsfc.nasa.gov/AIRS/documentation/v5_docs/AIRS_V5_Release_User_Docs/V5_L2_Standard_Product_QuickStart.pdf`.

Pierrehumbert, R., 1994: Tracer microstructure in the large-eddy dominated regime. *Chaos, Solitons & Fractals*, **4 (6)**, 1091–1110.

Pierrehumbert, R. and H. Yang, 1993: Global chaotic mixing on isentropic surfaces. *J. Atmos. Sci*, **50 (15)**, 2462–2480.

Pierrehumbert, R. T., 1996: Anomalous scaling of high cloud variability in the tropical Pacific. *Geophys. Res. Lett.*, **23 (10)**, 1095–1098.

Pressel, K. G., W. Collins, and A. Desai, 2010: Variance scaling in water vapor measurements from a tall tower. `http://ams.confex.com/ams/13CldPhy13AtRad/techprogram/paper_171839.htm`.

Pu, Z. and L. Zhang, 2010: Validation of Atmospheric Infrared Sounder temperature and moisture profiles over tropical oceans and their impact on numerical simulations of tropical cyclones. *J. Geophys. Res*, **115 (D24)**, D24 114.

Sherwood, S., R. Roca, T. Weckwerth, and N. Andronova, 2010: Tropospheric water vapor, convection, and climate. *Rev. Geophys*, **48**.

Sparling, L. and J. Bacmeister, 2001: Scale dependence of tracer microstructure: Pdfs, intermittency and the dissipation scale. *Geophys. Res. Lett.*, **28 (14)**, 2823–2826.

Stolle, J., S. Lovejoy, and D. Schertzer, 2009: The stochastic multiplicative cascade structure of deterministic numerical models of the atmosphere. *Nonlin. Processes Geophys*, **16**, 607–621.

Susskind, J., C. Barnet, and J. Blaisdell, 2003: Retrieval of atmospheric and surface parameters from AIRS/AMSU/HSB data in the presence of clouds. *Geoscience and Remote Sensing, IEEE Transactions on*, **41 (2)**, 390–409.

Tjemkes, S. and M. Visser, 1994: Horizontal variability of temperature, specific humidity, and cloud liquid water as derived from spaceborne observations. *J. Geophys. Res*, **99 (D11)**, 23 089–23.

Tobin, D., et al., 2006: Atmospheric Radiation Measurement site atmospheric state best esti-

mates for Atmospheric Infrared Sounder temperature and water vapor retrieval validation. *J. Geophys. Res*, **111**, D09S14.

Tuck, A., 2010: From molecules to meteorology via turbulent scale invariance. *Quart. J. Roy. Meteor. Soc.*, **136 (650)**, 1125–1144.

Tuck, A. and S. Hovde, 1999: Fractal behavior of ozone, wind and temperature in the lower stratosphere. *Geophys. Res. Lett.*, **26 (9)**, 1271–1274.

Tuck, A., S. Hovde, and M. Proffitt, 1999: Persistence in ozone scaling under the hurst exponent as an indicator of the relative rates of chemistry and fluid mechanical mixing in the stratosphere. *The Journal of Physical Chemistry A*, **103 (49)**, 10 445–10 450.

Waugh, D., 1996: Seasonal variation of isentropic transport out of the tropical stratosphere. *J. Geophys. Res.*, **101 (D2)**, 4007–4023.

Williams, P., 2005: Modelling climate change: the role of unresolved processes. *Philos. Trans. Roy. Soc. London A*, **363 (1837)**, 2931–2946.

Wood, A. and G. Chan, 1994: Simulation of stationary Gaussian processes in [0, 1] d. *Journal of Computational and Graphical Statistics*, **3 (4)**, 409–432.

Wood, R. and P. R. Field, 2011: The distribution of cloud horizontal sizes. *J. Climate*, **24**, 110429091151 046.

Wood, R. and J. P. Taylor, 2001: Liquid water path variability in unbroken marine stratocumulus cloud. *Quart. J. Roy. Meteor. Soc.*, **127**, 2635–2662.

Yang, H. and R. Pierrehumbert, 1994: Production of dry air by isentropic mixing. *J. Atmos. Sci.*, **51 (23)**, 3437–3437.

List of Tables

1 The mean $\bar{H}$, standard deviation σ, and boot-strapped 95% confidence intervals for land masked extratropical (between 20°S – 58°S and between 20°N – 58°N scaling exponents for which the absolute difference between along-track and across-track scaling exponents is less than 10% of the of the directionally independent structure function exponent value. Also given is the percentage of land masked structure function domains of directionally-independent, along-track, and across-track log-log structure function fits for which $R^2 > 0.95$, and for which the difference between along-track and across-track structure function exponents is less than 10% of the directionally-independent structure function exponent exponent value.

		925 hPa				500 hPa			
		H	σ	95% CI	% scaling	H	σ	95% CI	% scaling
DJF	ASC	0.335	0.047	(0.333, 0.337)	44.6	0.556	0.047	(0.555, 0.558)	71.1
	DES	0.396	0.064	(0.394, 0.397)	80.2	0.561	0.065	(0.558, 0.562)	84.0
JJA	ASC	0.334	0.032	(0.332, 0.335)	70.0	0.548	0.067	(0.546, 0.549)	83.1
	DES	0.379	0.049	(0.378, 0.381)	75.8	0.549	0.042	(0.548, 0.551)	91.2

TABLE 1. The mean $\bar{H}$, standard deviation σ, and boot-strapped 95% confidence intervals for land masked extratropical (between 20°S – 58°S and between 20°N – 58°N) scaling exponents for which the absolute difference between along-track and across-track scaling exponents is less than 10% of the of the directionally independent structure function exponent value. Also given is the percentage of land masked structure function domains of directionally-independent, along-track, and across-track log-log structure function fits for which $R^2 > 0.95$, and for which the difference between along-track and across-track structure function exponents is less than 10% of the directionally-independent structure function exponent exponent value.

List of Figures

1 Two synthetic Gaussian random processes (ϕ) having Hurst exponents of $H \approx 0.3$ and $H \approx 0.7$ in the top and bottom panels respectively. The inset plot in each figure shows the first order structure function computed from the random process. The Hurst exponent estimated by least squares regression is also denoted.

2 AIRS 500 hPa three month mean water vapor mass mixing ratio [g kg^{-1}] for Ascending (ASC) and Descending (DES) passes. Means were computed by binning individual retrievals to a 1.0° × 1.0° latitude-longitude grid. Masked values, appearing in white, represent grid boxes for which there were no successful AIRS retrievals during the analysis period.

3 AIRS 925 hPa three month mean water vapor mass mixing ratio [g kg^{-1}]. Note the difference in colorbar between Figures 2 and 3. Means were computed by binning individual retrievals to a 1.0° × 1.0° latitude-longitude grid. Masked values, appearing in white, represent grids for which there were no successful AIRS retrievals during the analysis period.

4 Example 500 hPa DJF ascending pass Along-Track (Along), Across-Track (Across), and Directionally-Independent (DI) structure functions for a structure function domain centered centered at 165°W and 51°N. The selection of this particular structure function domain was arbitrary.

5 Maps of directionally-independent, across-track, and along-track scaling exponents (left, middle, and right column, respectively) for ascending (ASC) and descending (DSC) passes during December, January, and February 2007 -2008 for the 500 hPa (top two rows) and 925 hPa (bottom two rows) AIRS retrieval levels. Regions for which the $R^2 > 0.95$ quality of fit criterion are not met are indicated with black hatching.

6 Same as Figure 5 but for June, July and August 2008.

7 Zonal mean cross section of directionally-independent (left column), along-track (center column), and across-track (right column) scaling exponents for DJF 2007/2008 and JJA 2008 for all AIRS retrieval levels between 1000 hPa and 300 hPa. Scaling exponents determined from least squares fits with $R^2 < 0.95$ are not included in the computation of the zonal mean.

8 AIRS mean averaging kernels for the AIRS trapezoidal layers with effective pressure level closest to 925 hPa, 700 hPa and 500 hPa respectively for subtropical ocean (left column), tropical ocean (center column), and subtropical land (right column). Mean averaging kernels are the arithmetic mean for all vertical profiles within a 2° latitude-longitude box centered on the latitude-longitude points given in the plot titles.

9 Estimated PDFs of along-track scaling exponents excluding the tropics (20°N to 20°S) for JJA and DJF ascending and descending passes. Scaling exponents for domains with land fraction > 10% are not included in the density estimate. The vertical lines represent reference values of 1/3 and 1/2.

10 Plots of $\log(q_v/\max q_v)$ where q_v is the water vapor mass mixing ratio for a single day's ascending passes for 500 hPa and 925 hPa. This normalization allows the maps at 500 hPa and 925 hPa to be plotted with a single colorbar and emphasizes the filimentary structure of the extratropical water vapor field.

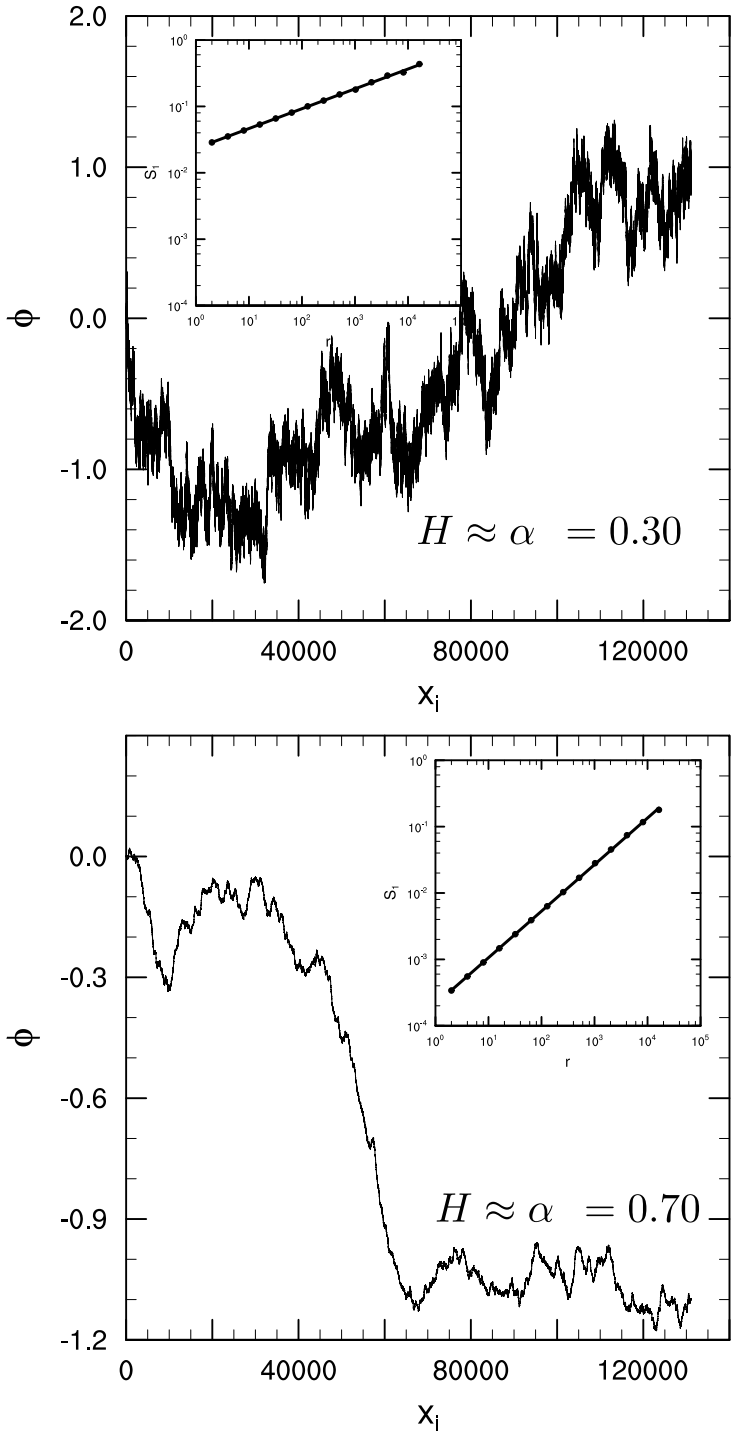

FIG. 1. Two synthetic Gaussian random processes (ϕ) having Hurst exponents of $H \approx 0.3$ and $H \approx 0.7$ in the top and bottom panels respectively. The inset plot in each figure shows the first order structure function computed from the random process. The Hurst exponent estimated by least squares regression is also denoted.

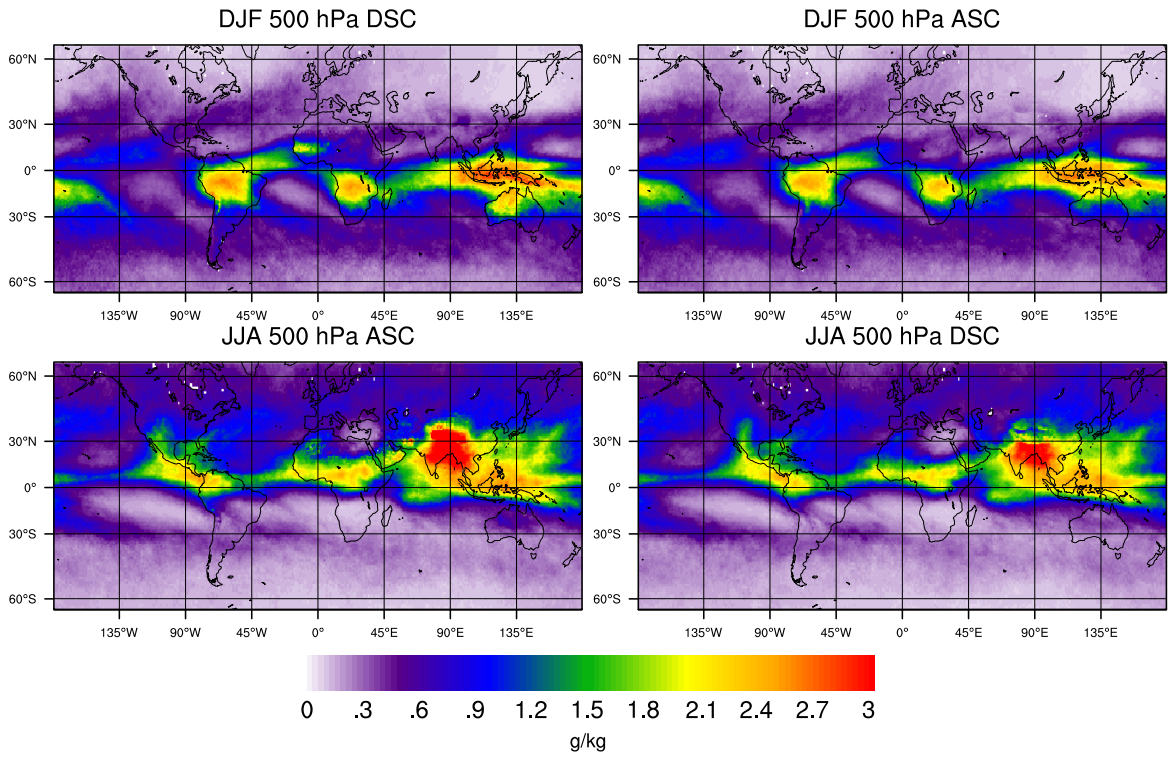

FIG. 2. AIRS 500 hPa three month mean water vapor mass mixing ratio [g kg^{-1}] for Ascending (ASC) and Descending (DES) passes. Means were computed by binning individual retrievals to a 1.0° × 1.0° latitude-longitude grid. Masked values, appearing in white, represent grid boxes for which there were no successful AIRS retrievals during the analysis period.

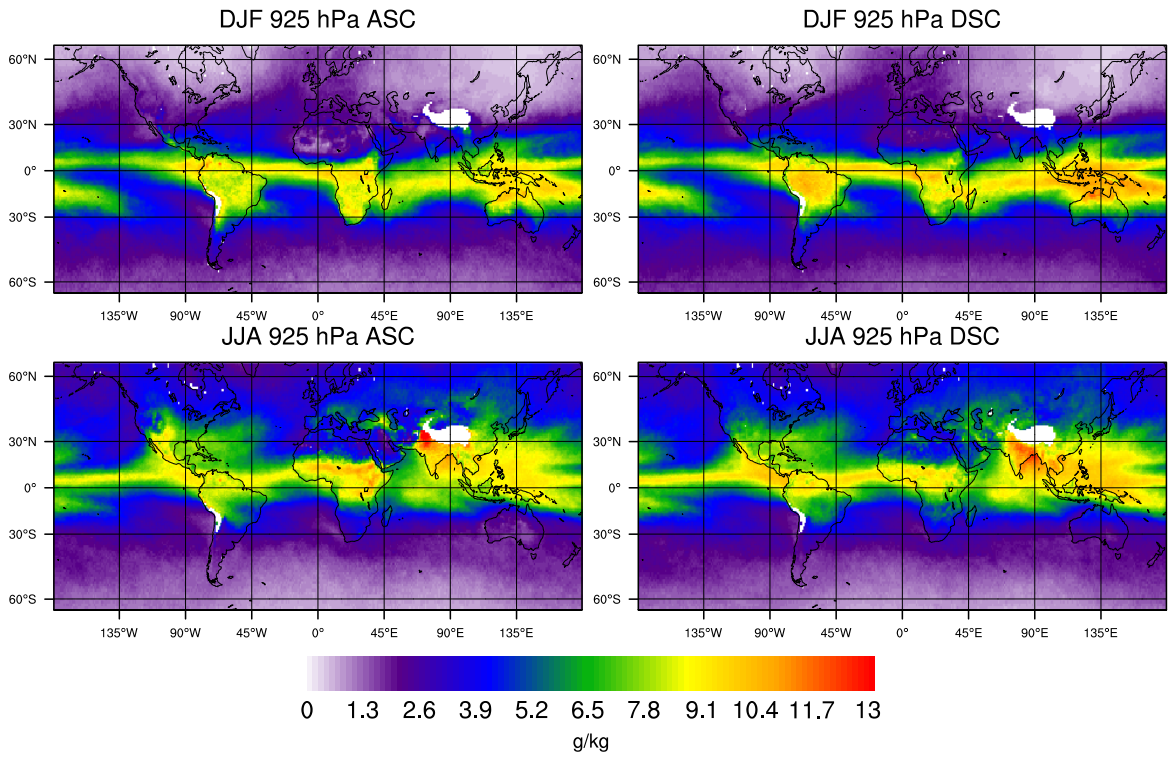

FIG. 3. AIRS 925 hPa three month mean water vapor mass mixing ratio [g kg^{-1}]. Note the difference in colorbar between Figures 2 and 3. Means were computed by binning individual retrievals to a 1.0° × 1.0° latitude-longitude grid. Masked values, appearing in white, represent grids for which there were no successful AIRS retrievals during the analysis period.

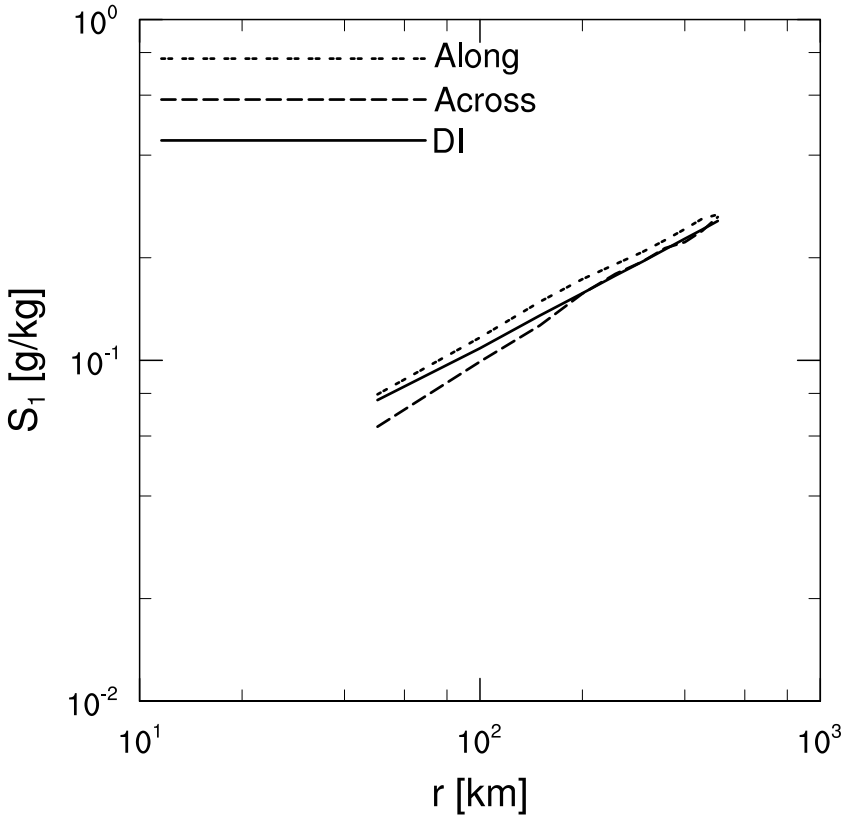

FIG. 4. Example 500 hPa DJF ascending pass Along-Track (Along), Across-Track (Across), and Directionally-Independent (DI) structure functions for a structure function domain centered centered at 165°W and 51°N. The selection of this particular structure function domain was arbitrary.

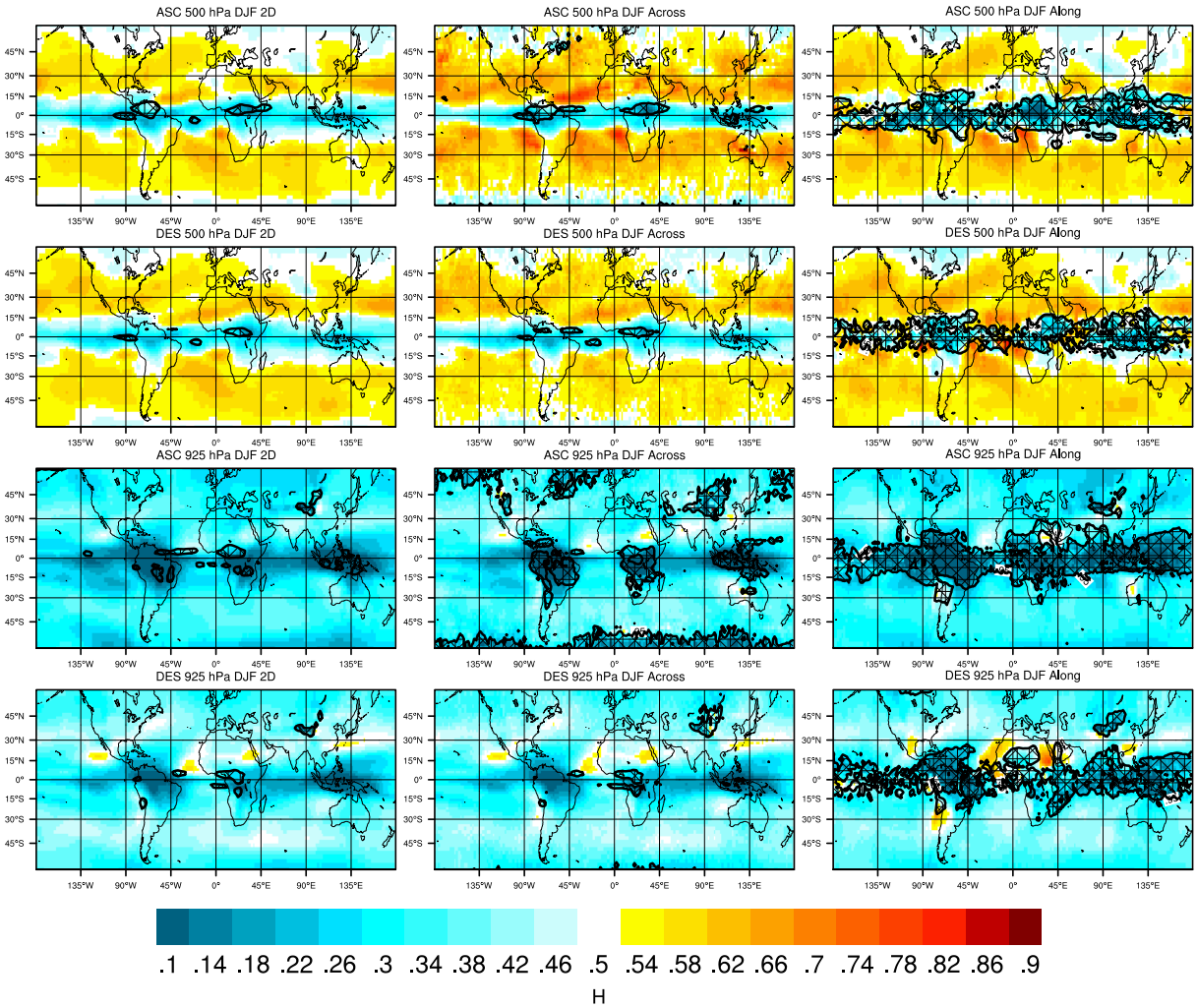

FIG. 5. Maps of directionally-independent, across-track, and along-track scaling exponents (left, middle, and right column, respectively) for ascending (ASC) and descending (DSC) passes during December, January, and February 2007 -2008 for the 500 hPa (top two rows) and 925 hPa (bottom two rows) AIRS retrieval levels. Regions for which the $R^2 > 0.95$ quality of fit criterion are not met are indicated with black hatching.

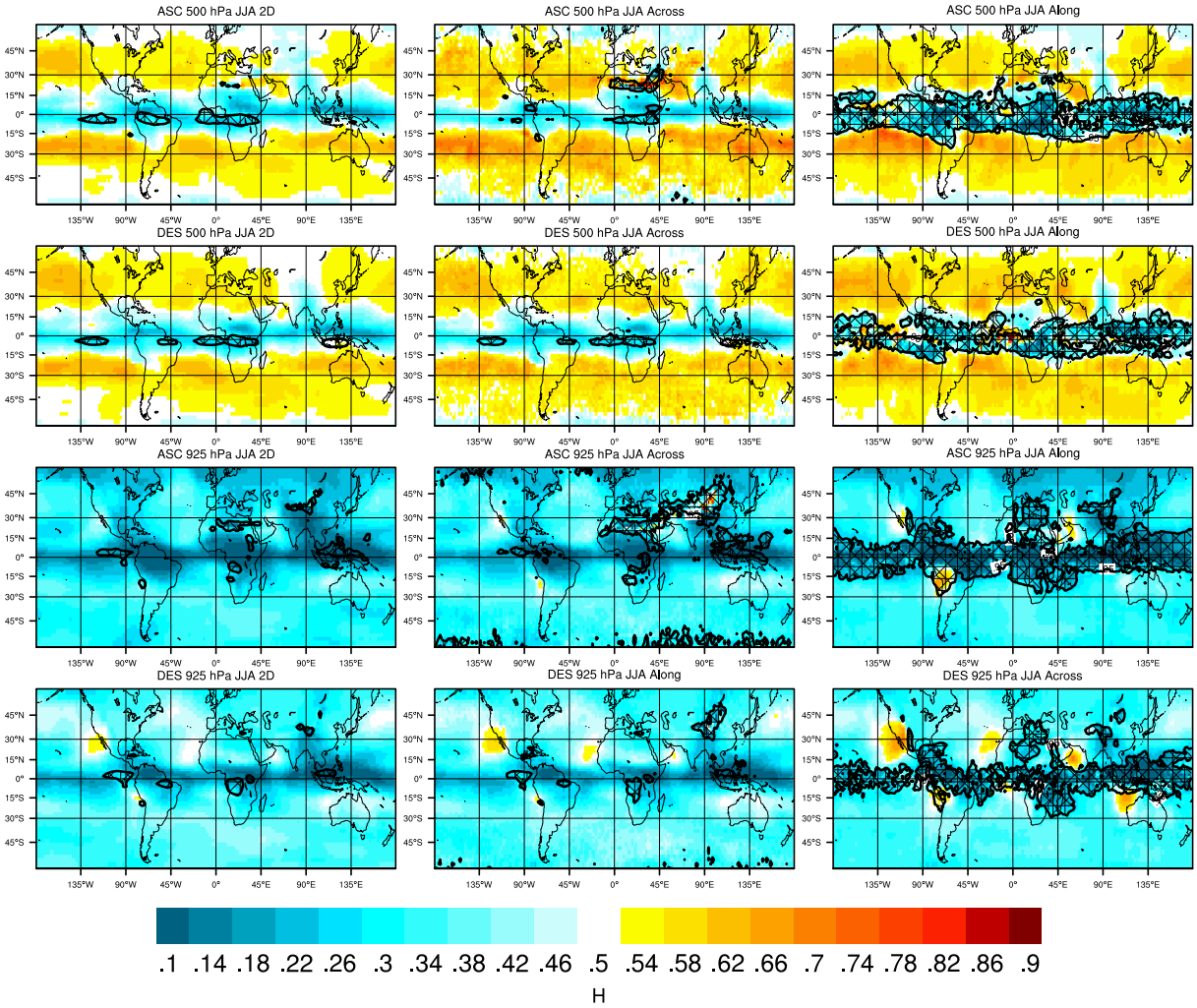

FIG. 6. Same as Figure 5 but for June, July and August 2008.

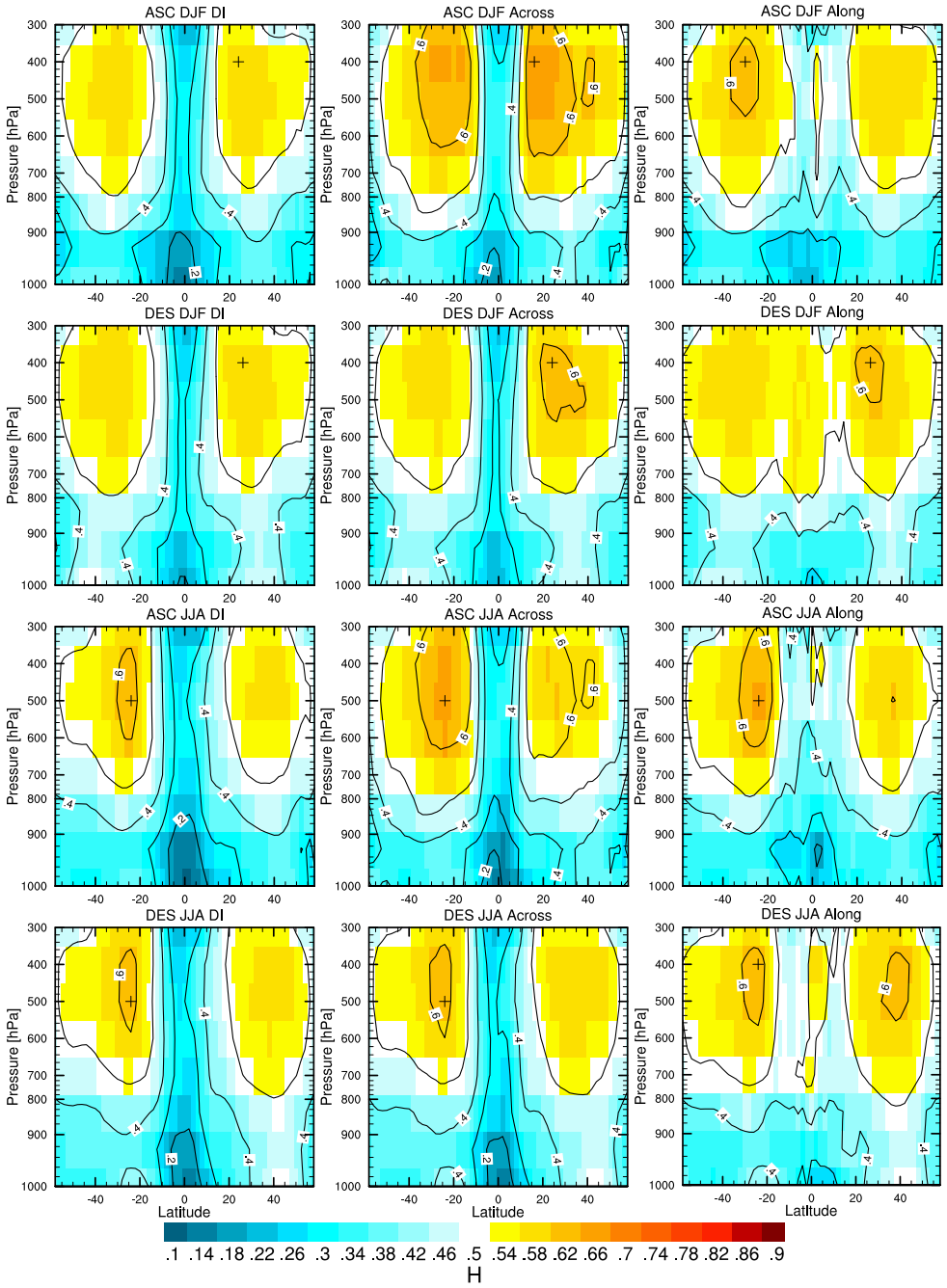

FIG. 7. Zonal mean cross section of directionally-independent (left column), along-track (center column), and across-track (right column) scaling exponents for DJF 2007/2008 and JJA 2008 for all AIRS retrieval levels between 1000 hPa and 300 hPa. Scaling exponents determined from least squares fits with $R^2 < 0.95$ are not included in the computation of the zonal mean.

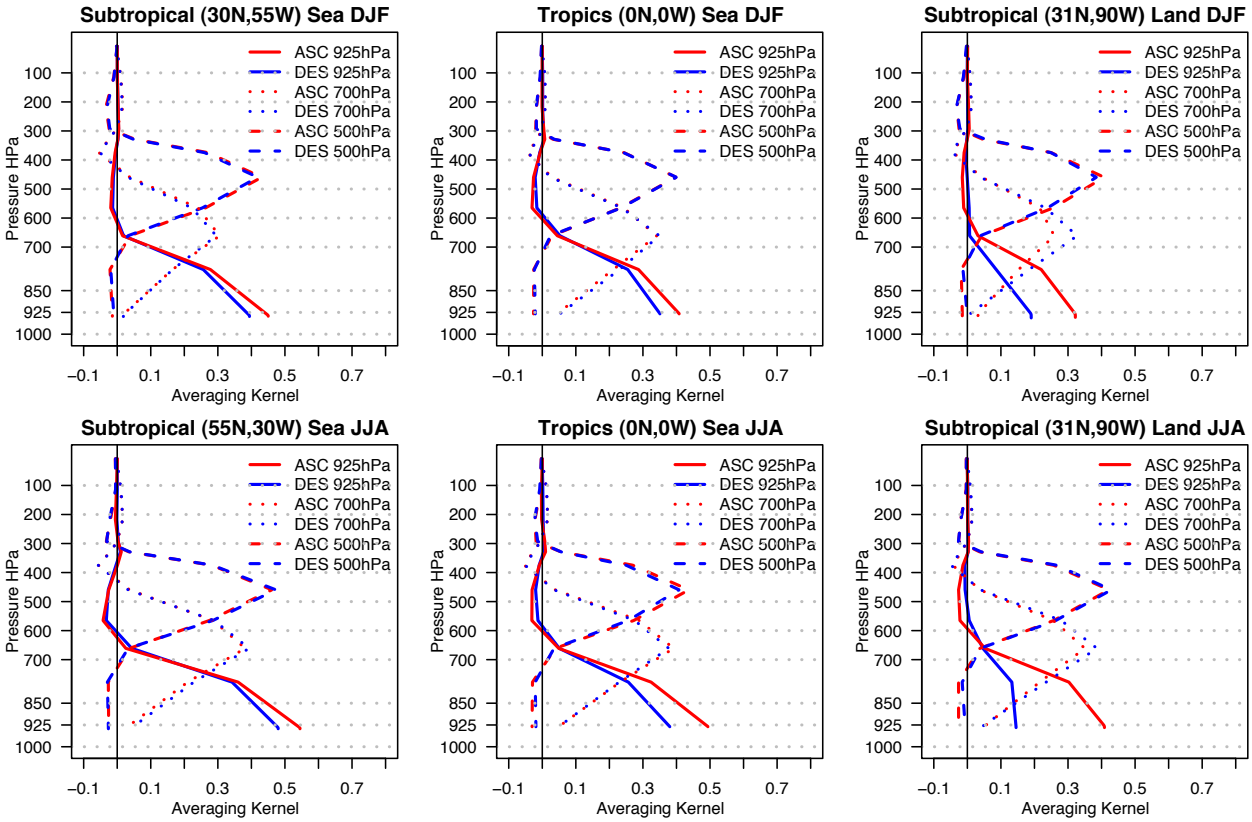

FIG. 8. AIRS mean averaging kernels for the AIRS trapezoidal layers with effective pressure level closest to 925 hPa, 700 hPa and 500 hPa respectively for subtropical ocean (left column), tropical ocean (center column), and subtropical land (right column). Mean averaging kernels are the arithmetic mean for all vertical profiles within a 2° latitude-longitude box centered on the latitude-longitude points given in the plot titles.

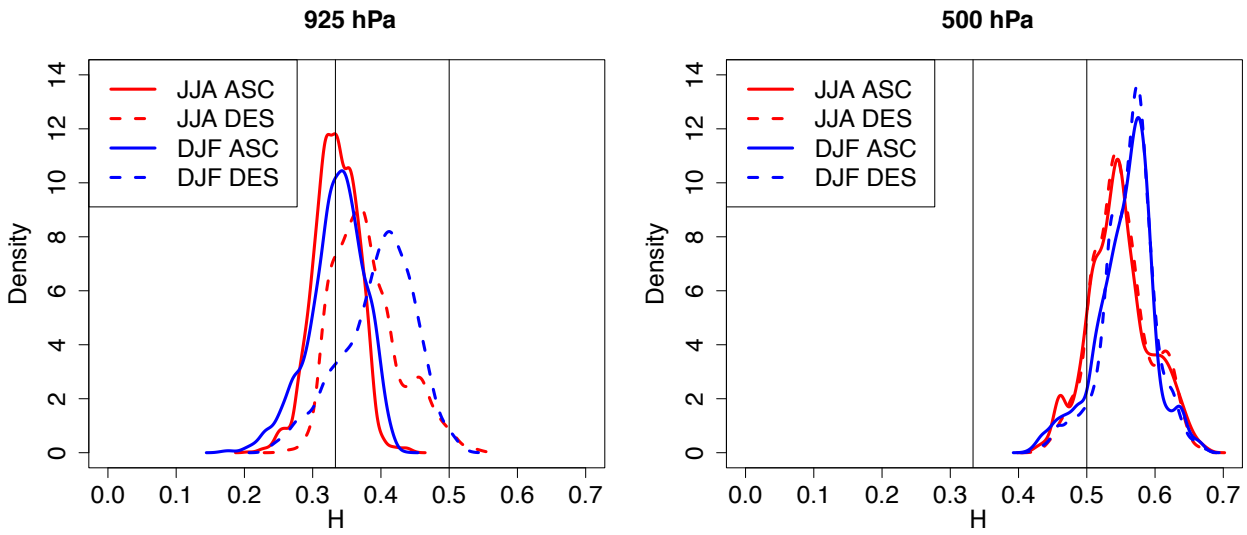

FIG. 9. Estimated PDFs of along-track scaling exponents excluding the tropics (20°N to 20°S) for JJA and DJF ascending and descending passes. Scaling exponents for domains with land fraction > 10% are not included in the density estimate. The vertical lines represent reference values of 1/3 and 1/2.

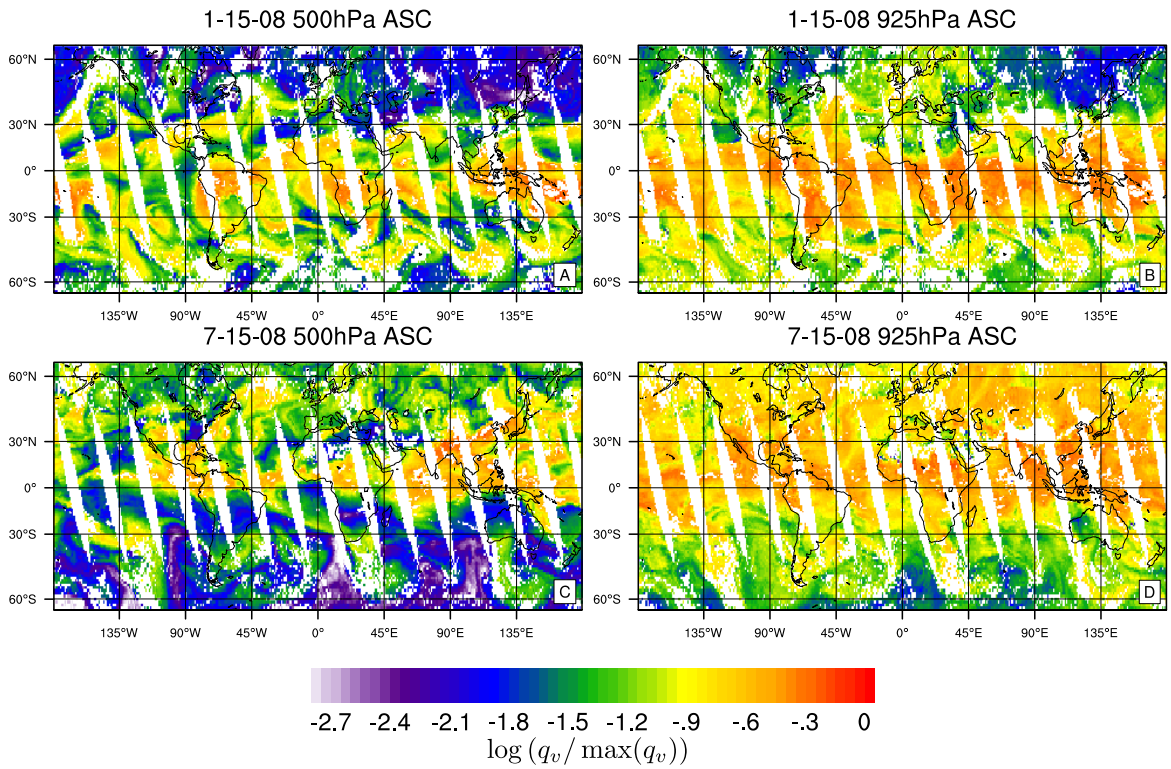

FIG. 10. Plots of $\log(q_v/\max q_v)$ where q_v is the water vapor mass mixing ratio for a single day's ascending passes for 500 hPa and 925 hPa. This normalization allows the maps at 500 hPa and 925 hPa to be plotted with a single colorbar and emphasizes the filimentary structure of the extratropical water vapor field.

DISCLAIMER

This document was prepared as an account of work sponsored by the United States Government. While this document is believed to contain correct information, neither the United States Government nor any agency thereof, nor The Regents of the University of California, nor any of their employees, makes any warranty, express or implied, or assumes any legal responsibility for the accuracy, completeness, or usefulness of any information, apparatus, product, or process disclosed, or represents that its use would not infringe privately owned rights. Reference herein to any specific commercial product, process, or service by its trade name, trademark, manufacturer, or otherwise, does not necessarily constitute or imply its endorsement, recommendation, or favoring by the United States Government or any agency thereof, or The Regents of the University of California. The views and opinions of authors expressed herein do not necessarily state or reflect those of the United States Government or any agency thereof or The Regents of the University of California.

Ernest Orlando Lawrence Berkeley National Laboratory is an equal opportunity employer.